Infrared thermography of evaporative fluxes and dynamics of salt deposition on heterogeneous porous surfaces

Uri Nachshon,[1] Ebrahim Shahraeeni,[2,3] Dani Or,[2] Maria Dragila,[4] and Noam Weisbrod[1]

Received 10 April 2011; revised 7 November 2011; accepted 8 November 2011; published 16 December 2011.

[1] Evaporation of saline solutions from porous media, common in arid areas, involves complex interactions between mass transport, energy exchange and phase transitions. We quantified evaporation of saline solutions from heterogeneous sand columns under constant hydraulic boundary conditions to focus on effects of salt precipitation on evaporation dynamics. Mass loss measurements and infrared thermography were used to quantify evaporation rates. The latter method enables quantification of spatial and temporal variability of salt precipitation to identify its dynamic effects on evaporation. Evaporation from columns filled with texturally-contrasting sand using different salt solutions revealed preferential salt precipitation within the fine textured domains. Salt precipitation reduced evaporation rates from the fine textured regions by nearly an order of magnitude. In contrast, low evaporation rates from coarse-textured regions (due to low capillary drive) exhibited less salt precipitation and consequently less evaporation rate suppression. Experiments provided insights into two new phenomena: (1) a distinct increase in evaporation rate at the onset of evaporation; and (2) a vapor pumping mechanism related to the presence of a salt crust over semidry media. Both phenomena are related to local vapor pressure gradients established between pore water and the surface salt crust. Comparison of two salts: NaCl and NaI, which tend to precipitate above the matrix surface and within matrix pores, respectively, shows a much stronger influence of NaCl on evaporation rate suppression. This disparity reflects the limited effect of NaI precipitation on matrix resistivity for solution and vapor flows.

Citation: Nachshon, U., E. Shahraeeni, D. Or, M. Dragila, and N. Weisbrod (2011), Infrared thermography of evaporative fluxes and dynamics of salt deposition on heterogeneous porous surfaces, *Water Resour. Res.*, *47*, W12519, doi:10.1029/2011WR010776.

1. Introduction

[2] Quantifying water evaporation from terrestrial surfaces is important for understanding key natural and engineered processes relevant to water management, global water cycle, soil and groundwater salinization, food and building industries and more. Numerous studies have explored evaporation from bare homogeneous soils under natural [e.g., *Ben-Asher et al.*, 1983; *Blight*, 2002; *Evett et al.*, 1994; *Penman*, 1948] and agricultural conditions [e.g., *Daamen et al.*, 1995; *Van Wesemael et al.*, 1996]. Nevertheless, very little is known about evaporation from heterogeneous porous media in general and in particular with the added effect of salt precipitation during the evaporation process. Recently, *Lehmann and Or* [2009] investigated the physics of water evaporation from heterogeneous porous media with a sharp vertical textural interface. The authors reported higher evaporation from the heterogeneous porous media than from its homogeneous counterpart. The spatial distribution of evaporative fluxes from such heterogeneous surfaces was quantified by *Shahraeeni and Or* [2010] using infrared thermography (IRT). It was shown that heterogeneity induces internal capillary flows between domains that result in higher values of evaporation through the finer sand, while the contribution of the coarse sand surfaces to average evaporation rate from the system was relatively minor.

[3] While the studies cited above explored evaporation of salt-free water, under many natural conditions, pore water may contain appreciable amounts of dissolved salts. Therefore, understanding the dynamics and impact of salt accumulation and precipitation on the evaporation process is crucial. Salt precipitation during evaporation and its effect on evaporation has been examined for homogeneous conditions [e.g., *Fujimaki et al.*, 2006; *Nassar and Horton*, 1999; *Shimojima et al.*, 1996] and for evaporation from fractures [*Weisbrod et al.*, 2005; *Kamai et al.*, 2009]. Salt was found to reduce evaporation as solution osmotic potential increased and matrix pores became gradually blocked due to salt crystal precipitation, which reduced the vapor diffusion coefficient through the matrix. Saline evaporation under heterogeneous conditions with a receding drying front was recently investigated by *Nachshon et al.* [2011]. In this work salt was found

[1]Department of Environmental Hydrology and Microbiology, Zuckerberg Institute for Water Research, Jacob Blaustein Institutes for Desert Research, Ben-Gurion University of the Negev, Midreshet Ben-Gurion, Israel.
[2]Institute of Terrestrial Ecosystems, Department of Environmental Science, ETH Zurich, Zurich, Switzerland.
[3]Institute of Fluid Dynamics, Department of Mechanical and Process Engineering, ETH Zurich, Zurich, Switzerland.
[4]Faculty of Soil Science, School of Integrated Plant, Soil and Insect Sciences, Oregon State University, Corvallis, Oregon, USA.

0043-1397/11/2011WR010776

to deposit primarily in the small pore and fine textured areas of the matrix.

[4] Evaporation often involves formation of a receding drying front especially in soils with a deep water table [*Fisher*, 1923]. The intrinsic reduction in evaporation rates (ER) and formation of internal vaporization planes complicate the study of impacts of salt deposition on evaporation dynamics. Another experimental challenge is how to resolve and distinguish variations in evaporation rates and associated salt deposition from heterogeneous surfaces. Our goal was to quantify evaporation of saline solutions and associated salt precipitation patterns and rates in homogeneous and heterogeneous porous media. We employed IRT measurements to enable, for the first time, quantification of the spatial distribution of evaporation rates from porous media under saline conditions. Measurements were done under constant hydraulic head conditions; i.e., no changes in liquid phase distribution and in the location of vaporization plane at the surface. This approach enabled for the first time to isolate and quantify the salt effect on evaporation, without complications resulting from receding drying front.

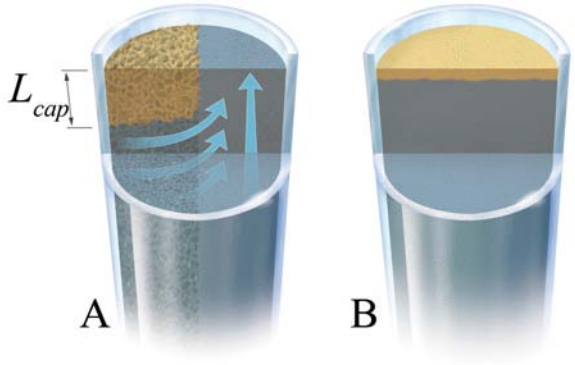

Figure 1. Conceptual illustration of the evaporation process from (a) a heterogeneous matrix, and (b) a homogeneous matrix. L_{cap} represents the height difference in water level between the fine and coarse sections, which reflects the air-entry pressure difference between the two media [after *Lehmann and Or*, 2009]. Blue and yellow regions indicate saturated and dry portions of the matrix, respectively. Arrows indicate liquid flow from coarse to fine sections.

2. Theory

2.1. Evaporation From Homogeneous and Heterogeneous Porous Media Under Saline Conditions

[5] *Fisher* [1923] described the evaporation of nonsaline water from homogeneous porous media in the absence of a constant water supply or in the case of a deep water table as a process occurring in three stages. *Lehmann et al.* [2008] further elaborated on the first and second stages of evaporation for well sorted sand, as used in the present study. The stages are defined as follows: Stage 1 (S1) is often characterized by a constant high ER, and continues as long as there is hydraulic capillary continuity between a receding drying front and vaporization plane at the matrix surface; Stage 2 (S2) begins when hydraulic continuity is disrupted and evaporation becomes limited by vapor diffusion through the porous medium; Stage 3 (S3) is characterized by a low ER, and is established when the evaporation front is deep below the matrix surface and evaporation is governed only by diffusive vapor transport.

[6] *Lehmann and Or* [2009] further elaborated on evaporation dynamics from heterogeneous porous media. They have shown that the first stage of evaporation is extended in heterogeneous media in comparison with homogeneous media. In a heterogeneous configuration, liquid preferentially flows upward through the fine sand section due to stronger capillary forces in this region in comparison to the coarse region (Figure 1a). Consequently, a drying front propagates preferentially down the coarse region (supplying liquid for evaporation from the fine-textured region), whereas for a homogeneous setup the drying front recedes uniformly (Figure 1b). An additional characteristic of heterogeneous media is that large textural contrasts within the matrix can result in dual evaporation conditions, where the fine medium remains at S1 while the coarse medium component exhibits S2 evaporation. *Lehmann et al.* [2008] and *Lehmann and Or* [2009] introduced a characteristic length (L_{cap}) (Figure 1a) which determines an intrinsic condition for the transition between S1 and S2 for the fine medium, where L_{cap} is proportional to the difference between air entry pressure in the coarse sand and the capillary pressure at the onset of residual water content in the fine sand (expressed as hydraulic head in length units). As long as the water table depth is deeper than the air entry value of the coarser medium, but less than L_{cap}, this dual stage evaporation process is sustained. For similar porous media configurations, *Nachshon et al.* [2011] showed that the spatial distribution of salt precipitation follows the same pattern of preferential evaporation process and accumulates over or in the fine textured media.

[7] In contrast with the classical stages of evaporation for nonsaline water, *Nachshon et al.* [2011] defined three new stages of evaporation for saline solutions: SS1, SS2 and SS3. SS1 exhibits a high ER with minor and gradual decrease, due to increasing osmotic potential. During SS2, ER falls progressively due to salt-crust formation; SS3 is characterized by a constant low ER. Even though phenomenologically similar to the well-defined classical evaporation stages for pure water (S1, S2 and S3), these stages correspond to different mechanisms. *Nachshon et al.* [2011] showed that for efflorescence salt precipitation (for NaCl) SS2 and parts of SS3 take place while matrix water content can still support first-stage evaporation (S1). While these three stages were quantified for conditions of a receding water table [*Nachshon et al.*, 2011], in the present work we quantify them for conditions of constant hydraulic head, thus the net effect of the salt precipitation is examined.

[8] *Nachshon et al.* [2011], as well as others [e.g., *Chen*, 1992; *Fujimaki et al.*, 2006; *Nassar and Horton*, 1999; *Shimojima et al.*, 1996; *Gran et al.*, 2011a] reported that as salt crust gradually forms over an evaporating porous surface, ER is reduced due to resistance of the salt crust to vapor transport. The studies cited above assumed that evaporation occurs below the precipitated salt crust. On the other hand, *Sghaier and Prat* [2009] explored experimentally the evaporation of an aqueous NaCl solution from porous media and concluded that evaporation is taking place on top of the salt crust. Moreover, the authors reported significant increase in ER at the beginning of the evaporation

process, during the formation of the NaCl salt crust. This phenomenon was explained by strong capillary forces of the salt that increased solution capillary flow to the evaporation surface, which according to them occurs on top of the salt crust. For later stages of evaporation, *Sghaier and Prat* [2009] reported reduction in ER as the evaporation front recedes into the matrix and the hydraulic continuity between the solution and the salt crust ceased.

[9] Since the studies cited above were done for transient hydraulic conditions with a receding evaporation front conditions it is difficult to distinguish salt crust effects on evaporation dynamics from hydraulic alterations due to the receding drying front. It follows from *Sghaier and Prat* [2009] that while hydraulic continuity between the solution and the precipitated salt crust is maintained, ER should not be reduced by the solution's capillary flow through the salt crust. The work presented here permits testing of this implication as experiments were done for constant hydraulic head conditions.

[10] Salt precipitation patterns may alter evaporation dynamics. Two patterns of salt precipitation are common in porous media: subflorescence where salt precipitates below the matrix surface within the pores, and efflorescence in which a crust forms above the surface [*Rodriguez-Navarro and Doehne*, 1999]. Formation of these patterns depends on salt species, humidity and thermal conditions [*Rodriguez-Navarro and Doehne*, 1999]. Efflorescent crusts deposit during S1, when the solution evaporates at the surface, therefore its effect on evaporation starts during early stages of the evaporation process. When salt is precipitated as subflorescence, its primary effect becomes evident during SS2 and SS3, due to alteration of pore spaces available for flow and potential decrease in unsaturated hydraulic conductivity [*Wissmeier and Barry*, 2008] and vapor-diffusion coefficient of the matrix, due to reduction in matrix porosity [*Millington and Quirk*, 1961]. *Nachshon et al.* [2011] found that heterogeneity played an important role in circumventing much of the salt-related suppression of evaporation that was seen in homogeneous media. The segregation of evaporative fluxes and salt deposits to primarily finer sand inclusions leaves the surface of coarser sand relatively salt-free, and thus forming a bypass region for vapor diffusion. Additionally, the authors have shown [*Nachshon et al.*, 2011] that the vertical interface between the coarse and fine sand also contributes to the evaporation process as evidenced by a ~2-fold higher salt accumulation there compared to equivalent depths within the fine sand.

2.2. Thermography of Evaporation in the Presence of Salt Precipitation

[11] Infrared thermography has been used to quantify partitioning of the ER from different parts of a surface. It uses the thermal signature from the phase change to estimate evaporative mass flux. This technique was used by *Shahraeeni and Or* [2010] to calculate patterns of ER of distilled water (DI) from a heterogeneous surface based on the surface temperature measurement, and the method is explained in detail in their paper. In this method, surface temperature is remotely measured by the means of an infrared (IR) imager positioned to view the top of an evaporative surface, recording data at a specified time interval. Based on simple surface energy balance calculations, the rates of evaporative mass loss, and their spatial distribution can be deduced from the evolution of the surface temperature's spatial patterns and dynamics. *Shahraeeni and Or* [2011] measured the temperature field beneath an evaporative surface by taking side-view infrared images of an evaporating sand column and established a relationship between the penetration depth of the evaporative temperature perturbation and mass loss rates. Dimensional analysis of the energy balance equation in the work of *Shahraeeni and Or* [2011] yields the contribution of the storage term (dT/dt) much smaller than unity under normal environmental condition. This means that one can consider evaporation as a quasi-static process in which the time dependency of the medium's temperature can be eliminated.

[12] In this study, the IRT-based method is extended to consider salt mass deposition during evaporation. Modifications were made to the thermal technique to account for surface precipitation and crust formation. For the analysis it is assumed that the height of a precipitated crust increases at a constant rate that is proportional to cumulative evaporation and salt concentration in the pore solution. Furthermore we assume, based on the literature, that the salt crust surface is dry during the experiment with its height increasing by evaporation and salt precipitation that takes place below at the bottom of the salt crust [*Fujimaki et al.*, 2006; *Nachshon et al.*, 2011; *Nassar and Horton*, 1999; *Shimojima et al.*, 1996]. Therefore, the vaporization plane where phase change and energy exchange associated with latent heat of vaporization occurs at the sand surface beneath the salt crust. Quantification of the evaporation mass loss from the system requires careful calculation of the thermal field at various locations. In our calculations we use the following approach: For a homogeneous system, the temperature of the salt surface seen by the camera is used to estimate the temperature at the evaporation front located at the interface of the salt crust and the sand. A 1-D energy flux balance across the salt crust between these two interfaces is used to derive the relevant relationships. The same equations are used to estimate the temperature field of the fine-textured component of the heterogeneous sample, i.e., assuming only vertical fluxes. Lastly, the contribution from the coarse sand to the ER of that half of the column is calculated by performing an energy balance for a control volume of dry coarse sand, which gives the relationship between the temperature of the dry sand surface seen by the camera and that of the evaporation front deep below (at L_{cap}) the dry sand.

[13] For a homogeneous column an 'evaporation zone' is designated extending from the sand surface to a depth of a few centimeters below the surface that is thermally affected by evaporation. The temperature at the bottom of evaporation zone is equal to the initial matrix temperature unaffected by energy fluxes from or to the evaporation zone above. At the top of the evaporation zone, the energy required for phase change is consumed and the process results in the evaporative cooling of the evaporation zone and the salt crust above. The average temperature of the evaporation zone is defined by T_{sand}. The energy flux through the salt crust is calculated assuming thermal conduction across the crust thickness driven by temperature gradient between sand temperature (T_{sand}) and salt crust surface temperature (T_{salt}) measured by the IR camera. For

a quasi-steady (linear) temperature profile through the crust we obtain

$$\rho_{\text{water}} L_w e_0 = K_{\text{salt}} \frac{T_{\text{salt}} - T_{\text{sand}}}{\Delta L_{\text{salt}}}, \quad (1)$$

where ρ_{water} is water density (1000 kg m^{-3}), L_w is the latent heat of vaporization (2450 J kg^{-1}), e_0 is evaporation rate (m s^{-1}), K_{salt} is the heat conductivity of the salt crust (W m^{-1} K), T_{salt} (K) is the salt top surface temperature measured by IR camera, T_{sand} (K) is the average temperature of the sand in the evaporation zone and ΔL_{salt} is a time-dependent salt crust thickness (m).

[14] At the top boundary of the salt crust, the energy flux conducted from below is balanced by convective exchange with the air above according to

$$K_{\text{salt}} \frac{T_{\text{salt}} - T_{\text{sand}}}{\Delta L_{\text{salt}}} = h_a (T_\infty - T_{\text{salt}}), \quad (2)$$

where h_a is the convective heat transfer coefficient (W m^{-2} K) and T_∞ is the ambient air temperature (K) (Figure 2a). Here, h_a depends on the ambient airflow and could be calculated based on the Nusselt number. Equation (3) gives average Nusselt number for forced laminar airflow over flat plate considering its entire length [*Shahraeeni and Or*, 2011; *White*, 1991]:

$$\text{Nu} = \frac{h_a D}{k_a} = 0.664\,\text{Re}^{1/2}\,\text{Pr}^{1/3}, \quad (3)$$

for which D is a characteristic length taken in this study as the column diameter (m), k_a is the ambient air heat conductivity (W m^{-1} k), and Re and Pr are Reynolds and Prandtl numbers, respectively.

[15] Hence, with direct measurement of the salt crust top surface temperature (T_{salt}) we may calculate surface ER by eliminating the conduction term using equations (1) and (2):

$$e_0 = \frac{h_a}{\rho_{\text{water}} L_w} (T_\infty - T_{\text{salt}}). \quad (4)$$

[16] Since equation (2) relates crust thickness to T_{salt}, it can be used to estimate time-dependent crust thickness. Cumulative volume of evaporated water (assuming it is similar to the volume of solution) could be retrieved by integrating mass loss rate from the entire evaporating surface A over time. Having c (saline solution concentration by volume = 0.56 cm^3 of solid NaCl per 1 cm^3 of solution [*Schwartz and Myerson*, 2002]), the corresponding volume of salt can be calculated which gives the thickness of crust per surface area A. Substituting evaporation rate from equation (4) yields crust thickness as a function of top-crust surface temperature:

$$\Delta L_{\text{salt}}(t) = \int_0^t c e_0(t) dt = \int_0^t \frac{c h_a}{\rho_{\text{water}} L_w} [T_\infty - T_{\text{salt}}(t)] dt. \quad (5)$$

[17] Therefore one may measure ambient air temperature (T_∞) and salt surface temperature during a certain time interval $T_{\text{salt}}(t)$ to calculate crust thickness $\Delta L_{\text{salt}}(t)$ from equation (5).

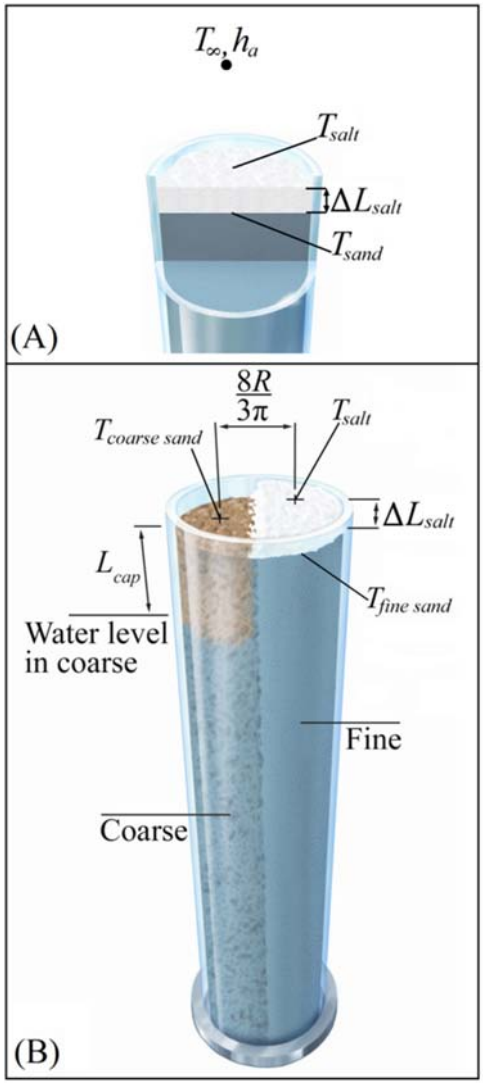

Figure 2. Schematic of the crust forming process in the case of a homogeneous column (Figure 2a) and heterogeneous column (Figure 2b). Blue color indicates saturated media. White on top of fine sand is the precipitated salt layer of thickness ΔL_{salt}. (a) Temperature at the top of salt crust is T_{salt} and at the bottom of salt crust (on the sand surface) is T_{sand}. Ambient air condition is specified by ambient air temperature T_∞ and convective heat transfer coefficient h_a. (b) Crust forming process in the case of a heterogeneous column. Temperature of fine and coarse volumes of sand are $T_{\text{fine sand}}$ and $T_{\text{coarse sand}}$, respectively. T_{salt} and $T_{\text{coarse sand}}$ are measurable by IR camera.

[18] Extracting ER data of a texturally heterogeneous surface, such as for a cylindrical column filled with half fine and half coarse media, saturated with NaCl (Figure 2b), requires more mathematical manipulation. For the fine-textured portion of the column, the same analysis as explained for the case of a homogeneous sample is applied, with equation (2) used to find the temperature at the top of the fine sand (below the salt crust).

$$T_{\text{fine sand}} = \frac{h_a \Delta L_{\text{salt}}}{K_{\text{salt}}}(T_\infty - T_{\text{salt}}) + T_{\text{salt}}. \quad (6)$$

[19] Evaporation from the coarse sand half takes place below the surface at depth L_{cap} where the water level is located. Since the diffusive flux is considerably smaller relative to capillary supported evaporation from the fine textured half, the evaporation process may not leave a significant thermal signature. An infrared image of the surface gives T_{salt} (top-crust surface temperature over the fine part of the column) and $T_{\text{coarse sand}}$ (coarse part surface temperature). Ambient air temperature T_∞ is independently measured.

[20] Estimation of ER contribution from the coarse part of the column could be done in several ways, for example, one may write an energy balance equation for control volume of coarse sand (Figure 2b) with height L_{cap} which is in contact with an equal volume of fine sand (to the right). Evaporation at a depth of L_{cap} lowers the temperature at that depth which is partly sensed at the top surface as $T_{\text{coarse sand}}$. But, for the sake of simplicity, variation of temperature along the vertical direction is eliminated within the coarse part and the temperature of the coarse sand volume above L_{cap} is assumed at a uniform $T_{\text{coarse sand}}$ measurable by IR camera. Naturally, this assumption introduces some errors in the ER estimation of dry surfaces where phase change does not take place at the surface. The layer of dry sand attenuates and dissipates part of the energy flux and induces some (strong) noise on the measurement. Moreover, water condensation below the matrix surface [*Gran et al.*, 2011a, 2011b] may decrease temperature difference between top sand surface and evaporation plane (at L_{cap}), which to some extent, reduces the simplification error. We also assume the column wall is an insulated boundary that does not let energy flow in or out of control volume. Therefore, energy fluxes to the control volume are evaporation from below, lateral conduction between coarse and fine regions and convection from the top. Lateral exchange is calculated by placing two nodes kept at $T_{\text{coarse sand}}$ and $T_{\text{fine sand}}$ located at the center of mass of each respective control volume. The energy balance equation becomes

$$\begin{aligned} &Q_{\text{conduction}} + Q_{\text{evaporation}} + Q_{\text{convection}} = 0 \\ &\frac{3\pi K_{\text{sand}}}{8R}(T_{\text{coarse sand}} - T_{\text{fine sand}}) + \rho_{\text{water}} L_w e_{0\text{coarse}} \\ &\quad = h_a(T_\infty - T_{\text{coarse sand}}). \end{aligned} \quad (7)$$

[21] Thermal conductivity of the partially saturated soil (K_{sand}) is a function of porosity and saturation which could be calculated based on the conductivity of water and dry sand. The same principal could be applied for the estimation of the other parameters which depends on the phase distribution in the medium [*Shahraeeni and Or*, 2011]. Equation (8) gives the ER through the coarse part of the surface:

$$\begin{aligned} e_{0\text{coarse}} = &\frac{h_a}{\rho_{\text{water}} L_w}(T_\infty - T_{\text{coarse sand}}) \\ &- \frac{3\pi K_{\text{sand}}}{8R\rho_{\text{water}} L_w}(T_{\text{coarse sand}} - T_{\text{fine sand}}). \end{aligned} \quad (8)$$

[22] Calculations of ER curves from coarse and fine regions using equations (7) and (8) were performed for each infrared image taken. Note that setting $c = 0$ in these relations (equations (4), (5), (6)) yields the evaporation of nonsaline water (no salt crust).

3. Materials and Methods

[23] We measured evaporation from transparent Poly Vinyl Chloride (PVC) sand columns, 25 cm in height and 5 cm in diameter. The columns were packed in three different configurations: (1) Homogeneous fine sand (Homo-fine); (2) Homogeneous coarse sand (Homo-coarse); and (3) Heterogeneous (Hetero) columns (Figure 3). Hetero columns were filled with 50% each of fine and coarse sands with a single vertical sharp interface between these two textures (Figure 3c). Columns were packed by pouring sands from the top. To pack the heterogeneous columns, thin (2 mm) cardboard spacers were used to keep fine and coarse sands segments separate during packing. After packing, the spacers were pulled out and the columns were gently shaken to assure tight packing.

[24] Dune sand obtained from Carlo Bernasconi AG (Switzerland) was sieved to 0.1–0.3 mm and 1–1.7 mm for the fine and coarse sands, respectively. Water content and retention measurements were performed to determine the van Genuchten parameters, air entry pressure and porosity. Average pore radii were calculated from the air entry pressure values (Table 1).

[25] Ten columns were used. Nine were filled with sand and saturated with various solutions and one column was filled with DI (no sand) to measure potential evaporation (PE). Each column was connected from the bottom to a 250 mL Marriott bottle to maintain a constant hydraulic head. Marriott bottles were filled with three different solutions: DI, 25% NaCl and 33% NaI solutions (by weight). The sand-filled DI columns served as reference for the saline columns to enable quantification of the salt effect on evaporation. NaCl was chosen as it precipitates as efflorescent salt crust [*Rodriguez-Navarro and Doehne*, 1999] and as it

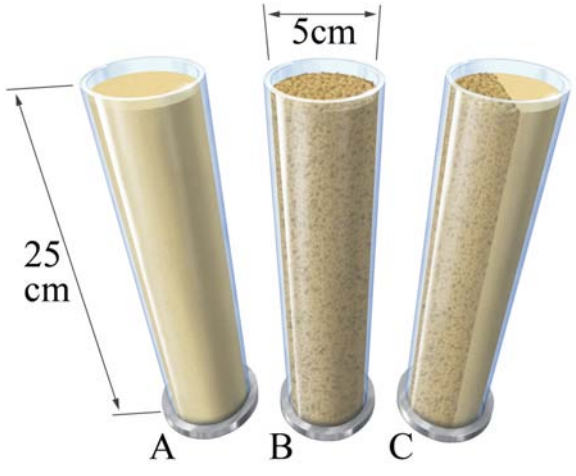

Figure 3. Column packing: (a) Homogeneous fine, (b) homogeneous coarse and (c) heterogeneous column divided into half fine sand next to coarse sand with a sharp vertical interface.

Table 1. Physical Properties of Sands

	Fine Sand	Coarse Sand
van Genuchten parameter (α)	2.753 1 m^{-1}	16.346 1 m^{-1}
van Genuchten parameter (N)	27.353	6.511
Porosity (ϕ_s)	0.364 m^3 m^{-3}	0.365 m^3 m^{-3}
Residual water content (ϕ_r)	0.064 m^3 m^{-3}	0.094 m^3 m^{-3}
Air entry pressure	35 cm	5 cm
Average pores radius (r)	41 μm	278 μm
Grain sizes range	0.1−0.3 mm	1−1.7 mm

is one of the most common salts in natural as well as man-made environments. NaCl solution concentration of 25% was chosen as it is very close to the NaCl saturation concentration in a solution (26% by weight). This high concentration suppresses changes in ER due to minute changes in solution concentration, permitting the assumption of constant NaCl solution concentration equal to saturation. Thus, all changes in ER for the NaCl columns are attributed to salt precipitation. NaI was chosen due to its tendency to precipitate as subflorescence below the evaporation front [*Nachshon et al.*, 2011]. We also considered the strong X-ray attenuation of NaI for subsequent CT scans [e.g., *Polak et al.*, 2003; *Zhu et al.*, 2007] to observe salt precipitation within pores. Details of CT scans of the NaI saturated matrix will be elaborated toward the end of section 3. NaI concentration of 33% by weight was chosen arbitrarily a value close to half of the NaI saturation concentration, hence in comparison with NaCl solution, a much higher amount of water loss is expected before NaI crystallization would begin. In other words, all the capillary pathways remain open for a longer duration compared to the NaCl solution and consequently, a much longer SS1 is expected.

[26] Marriott bottles were placed on Sartorius scales ED3202 (Sartorius AG, Germany) with an accuracy of ±0.01g to measure solution mass loss at 1 min intervals with data automatically stored on a computer. Surface temperatures of the columns were measured during evaporation by a SC6000 FLIR thermal camera (FLIR systems Inc., USA) with thermal Noise Equivalent Temperature Difference (NETD) less than 0.035K and spatial resolution of 375 μm. The camera's field of view, 19.2 cm × 24.1 cm, included all 9 sand columns. Images were taken every 30 min during the experiments.

[27] Marriott bottles maintained water table location at ∼6.5 cm below the top of the columns. The capillary fringe of the Homo-coarse medium was at a depth of 1.5 cm below sand surface, and the Homo-fine sand was saturated (under matric tension) up to the surface. This 1.5 cm difference was chosen as a compromise between the need to simulate evaporation from Hetero porous media with L_{cap} difference in water levels between fine and coarse pores, and the technical limitations of the thermal camera which would not be able to sense a much deeper evaporation front.

[28] Two PE were imposed, 2.4 cm d^{-1} and by blowing wind over the columns a rate of 3.84 cm d^{-1}, both measured using the DI-filled column. These PE values can be used to estimate PE from the saline solution at various concentrations using the Kelvin equation [*Alberty*, 1987; *Kelly and Selker*, 2001], knowing the solution activity, which can be found in the literature [*Stokes and Robinson*, 1949; *Robinson and Stokes*, 1959]. Experiment duration was 100 and 50 h for the low and high-PE cases, respectively. In addition, the Homo-fine NaCl column was left to evaporate for an additional 180 h beyond the initial 50 h. During these 180 h salt crust that precipitated on the sand surface was peeled off 5 times, at time intervals of approximately 24 h. The crust was peeled in order to determine whether the NaCl precipitated only as an efflorescent crust above the surface, and whether by removing it the initial ER returned, indicating that ER reduction was only due to vapor transport resistance of the salt crust. Concurrently, a Homo-coarse column was saturated with NaCl solution up to the surface and the salt crust precipitation was photographed in visible wavelengths to capture salt crust growth details. Figure 4 shows the experiment setup: it can be seen that duplicate columns of Hetero-NaCl were used. This repetition was done as the state of NaCl precipitation under heterogeneous conditions is the most interesting case for our research, thus experimental replicates were deemed important to validate these results. Mass data gave net ER per column, and thermal images provided the spatial distribution of the ER within each column, to discriminate the relative contribution of the fine and coarse segments within the Hetero columns.

[29] Following the end of the low ER experiment, a cylindrical subsample (1.5 cm in diameter and 5 cm in length) was extracted from the Hetero NaI column (including the fine-coarse boundary) and scanned by a CT scanner (μCT40, Scanco Medical AG, Switzerland) to determine the spatial distribution of salt precipitation within the matrix. Scans were done with X-ray energy of 70 kV, intensity of 114 μA and voxel size of 10 × 10 × 10 μm. CT post processing of scans was done using 3-D image analysis software (Avizo, Mercury, USA).

4. Results and Discussion

[30] Results are presented in terms of ER dynamics, which is the first derivative of the directly measured cumulative mass loss by evaporation. ER from sand-filled DI columns is presented first to isolate the effect of heterogeneity on evaporation from the salt effect. This is followed by results for NaCl and NaI to quantify the effect of efflorescent and subflorescent precipitation on evaporation rates. Finally, CT scans of the NaI sample reveal the spatial distribution of salt precipitation.

4.1. Evaporation From Sand-Filled DI Columns

[31] DI columns exhibited constant evaporation rates throughout the experiments (Figure 5), as expected for a constant water table depth and atmospheric boundary conditions. The fine sand (both for Homo and Hetero columns) exhibited evaporation rates ∼10 and ∼3 times higher than the coarse sand for the high- (H) and low- (L) PE conditions, respectively (Figure 5).

[32] Increased PE affected only the ER of the fine sand. A PE increase from 2.4 to 3.84 cm d^{-1} corresponded to an increase in ER by a factor of ∼3.5. By contrast, no significant increase was seen for the coarse media. The slightly higher ER of the coarse media for the lower PE (Figure 5e) may be due to inaccuracy in the evaporation front depth of this column which is affected by small changes in column sand packing and minor changes in the Marriott bottle

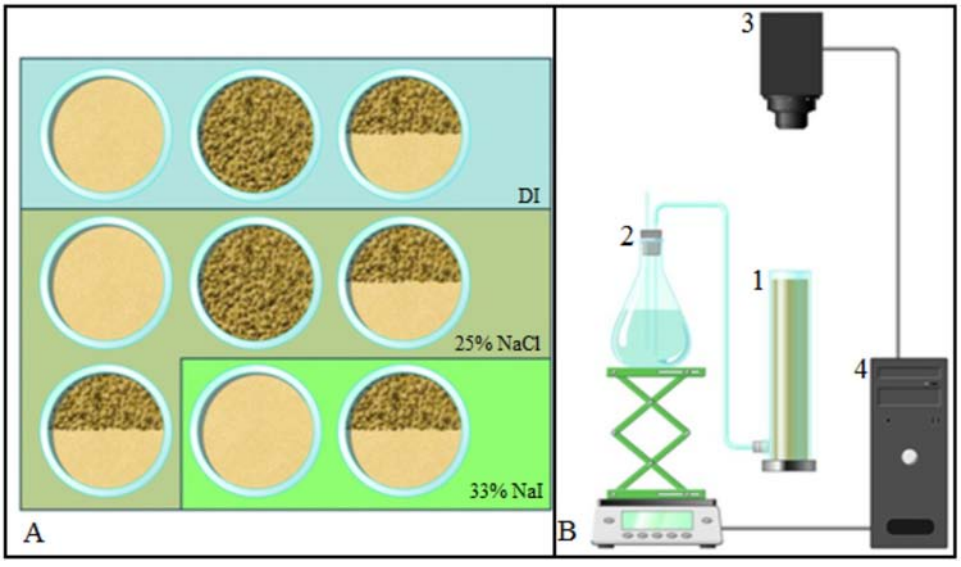

Figure 4. (a) Column setup. Homogeneous fine, homogeneous coarse and heterogeneous columns saturated with DI, 25% NaCl and 33% NaI. (b) Experiment setup. (1) Sand columns, (2) Marriott bottles on scales, (3) FLIR camera and (4) computer which collects mass and FLIR data.

installation. The lack of wind effect for the coarse media indicates that the wind did not induce advective ventilation of the coarse sand pores near the evaporation front, 1.5 cm below matrix surface.

[33] In the Hetero column, as expected according to *Lehman and Or* [2009], evaporation occurred preferentially from the finer sand fraction. The low ER in the coarse sand sections reflected rates supported primarily by vapor diffusion. Evaporation rates for DI columns were used as a reference for comparison with evaporation from saline columns with associated salt effects. The maximum DI evaporation rates for the fine and coarse sands were 3.2 $\pm$ 0.2 and 0.33 $\pm$ 0.3 cm d^{-1}, respectively. Evaporation rates measured below these values for similar PE for the other columns are thus exclusively due to salinity effects on the evaporation process.

4.2. Evaporation From NaCl Columns

[34] Results presented in Figure 6 depict measured ER from the NaCl columns, for high- and low-PE conditions. The IR temperature data for the Hetero columns clearly showed that most of the evaporation occurs over the fine

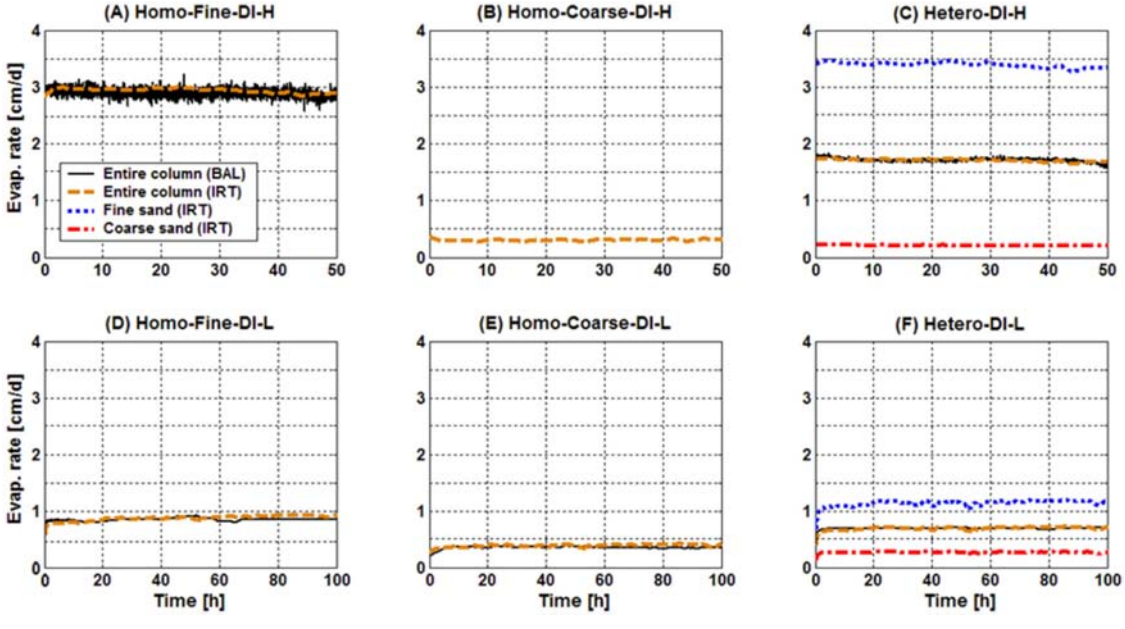

Figure 5. Evaporation rates for DI columns. Solid black lines are from balance readings (BAL), broken lines are for IRT readings (IRT) and (H) and (L) designate high- and low-potential evaporation rates conditions, respectively. Figure 5b "BAL" data is missing due to technical limitations.

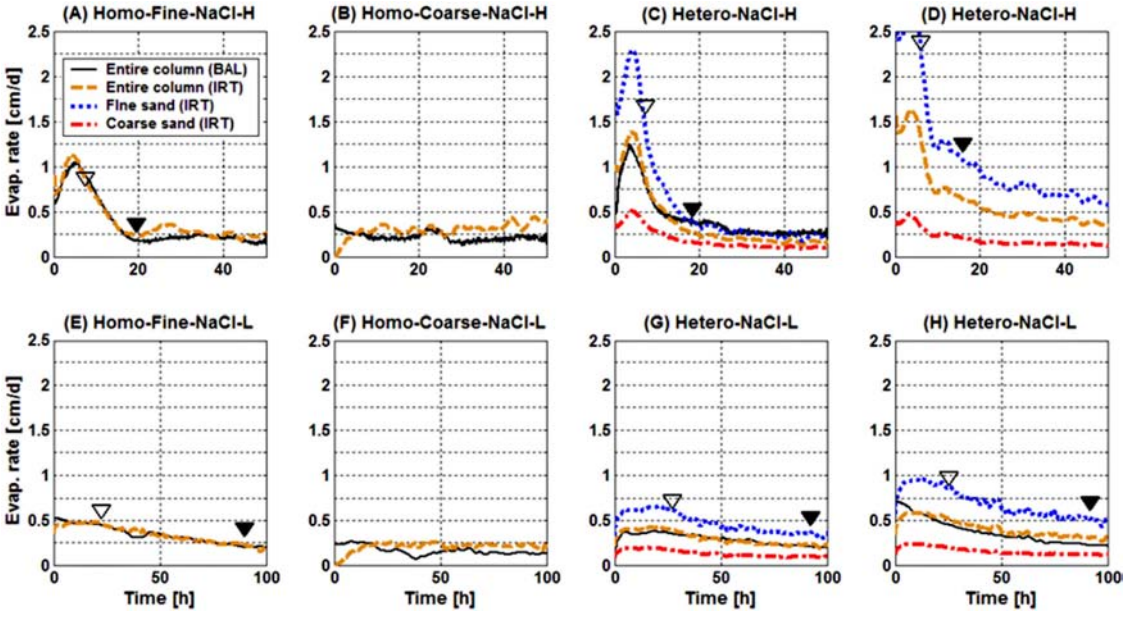

Figure 6. Evaporation rates for NaCl columns. Solid black lines are from balance readings (BAL), broken lines are for IRT readings (IRT) and H and L designate high- and low-potential evaporation rates conditions, respectively. White and black triangles indicate approximately the transitions between SS1-SS2 and SS2-SS3, respectively, of the fine sands. The differences between the Hetero columns (Figures 6c and 6d, and Figures 6g and 6h) reflect small uncontrolled environmental and physical changes between the duplicate heterogeneous columns.

sand sections. Consequently, salt accumulates over the fine section and reduces fine sand section's ER by an average factor of 4.4 and 2.4, for the high- and low-PE conditions, respectively. On the other hand, the coarse sand ER is less affected by the salt as it remains relatively free of salt crystals, with average ER reduced by a factor of 1.5 for both high- and low-PE conditions. The ER profiles in Figure 6 generally concur with the model presented by *Nachshon et al.* [2011] which predicts reduction in ER even when the porous medium is saturated. The authors defined the stages SS1, SS2, and SS3 to describe ER under saline conditions, for a receding drying front conditions. The same terminology is used here, while noting that SS2 and SS3 exhibit similar behavior for both stable and receding evaporation front cases, the first stage of evaporation for the stable evaporation front exhibits two additional interesting differences from the SS1 behavior of the receding drying front case of *Nachshon et al.* [2011]. For the receding drying front case, SS1 is characterized by an initially high ER that decreases moderately as the solution osmotic potential increase [*Nachshon et al.*, 2011] whereas in the case of a stable evaporation front, SS1 is characterized by a local increase but is not followed by the gradual decrease in ER (see time prior to white triangle marks in Figure 6). The lack of gradual decrease in ER is expected because the initial NaCl solution concentration used in these experiments is close to the solubility limit of NaCl, thus no significant increase in solution osmotic potential is expected which would result in such a decrease. The phenomenon of the initial local increase in ER, which reflects chemical and physical interactions between the solution and the precipitated salt crust will be elaborated shortly. Albeit these differences, the term SS1 is used as a general term to describe the first stage of evaporation under saline conditions.

[35] The nearly saturated initial concentration of NaCl solution supported the assumption that the osmotic potential of the solution did not change during the experiments, hence it is not expected to affect ER. Thus, the reduction in ER is attributed to reduction in vapor diffusion by formation of salt crust [*Fujimaki et al.*, 2006, *Nachshon et al.*, 2011]. The effective diffusion coefficient for water vapor through NaCl crust (D_s (m^2 s^{-1})) can be estimated from the measured ER during SS3. SS3 data is used because the low evaporation rate likely corresponds to a crust that is growing slowly. Salt crust thickness, L_{salt} is calculated using equation (5). Assuming that humid air below the salt crust is saturated with vapor (0.03 kg m^{-3}) and ambient air relative humidity above the salt crust is 50%, the vapor concentration difference ΔC_s is 0.015 kg m^{-3}. These parameters combined with measured vapor mass flux, J (kg s^{-1} m^2) can be used to calculate D_s using Fick's equation [*Bird et al.*, 2007, *Fick*, 1855].

$$J = -D_s \frac{\Delta C_s}{\Delta L_{salt}} \quad \Rightarrow \quad D_s = -J \frac{\Delta L_{salt}}{\Delta C_s}. \tag{9}$$

[36] Table 2 presents J, L_{salt}, ΔC_s and calculated D_s for all fine sand sections. Vapor diffusion coefficient in free air (D_{air}) at 25°C is equal to $2.6695 \cdot 10^{-5}$ m^2 s^{-1} [*Kimball et al.*, 1976], thus D_s is an order of magnitude smaller than D_{air}. Averaged D_s for the low PE conditions in these experiments is 1.8 times larger than D_s for high-PE conditions. This indicates that the precipitated salt crust resistance is not a constant but depends on environmental

Table 2. Data for Calculated D_s

		Homo-Fine	Hetero Fine 1	Hetero Fine 2
J (Kg s^{-1} m^2)	H[a]	3.47E-05	4.63E-05	5.79E-05
J (Kg s^{-1} m^2)	L[a]	1.74E-05	3.47E-05	4.63E-05
L_{salt} (m)	H	9.79E-04	4.89E-04	9.17E-04
L_{salt} (m)	L	1.65E-03	1.16E-03	1.71E-03
ΔC_s (Kg m^{-3})	H	0.015	0.015	0.015
ΔC_s (Kg m^{-3})	L	0.015	0.015	0.015
D_s (m^2 s^{-1})	H	1.16E-06	2.16E-06	2.31E-06
D_s (m^2 s^{-1})	L	1.74E-06	2.55E-06	6.17E-06

[a]H and L indicate high-and low-PE experiments, respectively.

conditions that may control the salt precipitation pattern. Consistent with this, *Nachshon et al.* [2011] found D_s to be 2 orders of magnitude smaller than D_{air}, applying PE of 1 cm d^{-1} with a receding evaporation front. It is well-established in literature that slow rate crystallization, usually, creates well organized, discrete big crystals, as opposed to high-rate crystallization, which yields crystals that are typically much smaller and more amorphous [*Press and Siever*, 1986; *Valeriani et al.*, 2005; *Mullin*, 2001; *Anderson*, 2000]. Under low PE conditions the crystals may accumulate at several discrete locations as well-developed crystals, leaving a large portion of the matrix surface free of salt. In contrast, under the high-PE conditions crystallization is likely to occur spontaneously all over the fine sand surface, resulting in homogeneous clogging of the surface. These two different salt precipitation patterns for high- and low-PE conditions were confirmed by visual observations (Figure 7). It is also known from literature that porosity of NaCl rocks, which is in the range of 1%–10%, is strongly affected by environmental conditions [*Beauheim and Roberts*, 2002; *Casas and Lowenstein*, 1989], and depends on salt crystallization conditions and degree of compaction. *Sghaier and Prat* [2009] reported on preliminary results of X-ray tomography from a NaCl efflorescence crust, showing the crust is highly porous with pores dimensions in the range of one to few tens μm. The wide range of D_s, measured here and by *Nachshon et al.* [2011] indicates the complex morphology of a precipitated salt crust. Further work is needed to quantitatively correlate PE conditions with the physical and hydraulic properties of the precipitated salt layer.

[37] IRT images are presented in Figure 8 for Homo-fine, Homo-coarse and Hetero NaCl columns, for the beginning of the evaporation process and 48 h later. The increase in average surface temperatures of ∼2 and ∼0.7°C, reflects a reduction of 30% and less than 10% in ER, for the fine and coarse sand sections, respectively.

[38] All columns (Figures 6a, 6c, 6d, 6e, 6g, and 6h), except the Homo-coarse columns (Figures 6b and 6f) showed local increase in ER during the first hours of the evaporation process. This was most prominent for the high-PE condition. This phenomenon was not observed for the DI and NaI columns, indicating that this may be related to the efflorescent salt crust formation process. This observation concurs with the results of *Sghaier and Prat* [2009] which have shown initially high evaporation rates from saline (NaCl) samples with the formation of efflorescence salt crust. These authors have interpreted the increase in ER as resulting from capillary suction of the solution by the salt, which lifts solution upward to the salt crust's upper surface. According to this concept, as long as there is hydraulic continuity between the solution and the precipitated salt crust the high ER should be sustained. But, in the results presented in here, the increase in ER sustained for few hours only (Figure 6), even though there was a continuous hydraulic continuity between the solution and the salt crust. Therefore, it is suggested that the capillary suction mechanism is probably not the key mechanism behind this observed increase in ER and an alternative mechanism is proposed. The alternative mechanism is related to vapor pressure gradients imposed between the solution and precipitated salt crust down chemical potential gradient between the two phases.

[39] *Scotter and Raats*, [1970], *Kelly and Selker* [2001], and *Weisbrod et al.* [2003] reported on salt generated vapor pressure gradient as a mechanism to drive water vapor in unsaturated soils. Gradients in soil-pore water osmotic pressure can result in significant flow of water (in vapor form) in soils under conditions of high solute concentrations and

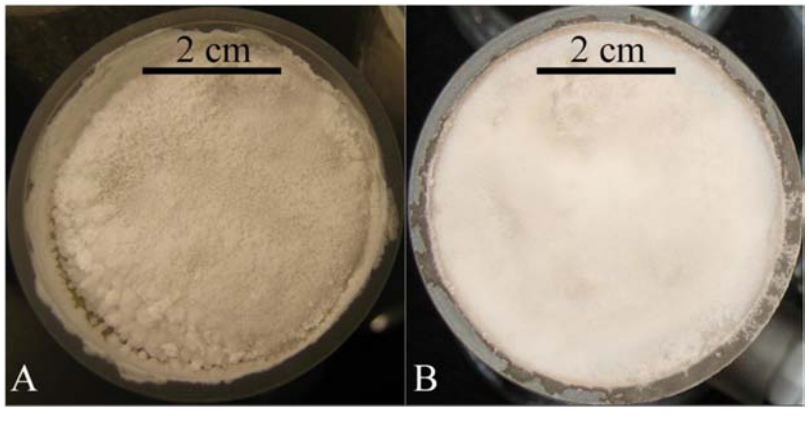

Figure 7. Salt precipitation over homogeneous NaCl columns. (a) Low and (b) high PE. Much larger, well developed crystals can be observed for low ER conditions, with part of the sand exposed to the atmosphere in the lower left side (Figure 7a) compared to homogeneous scattering of small salt crystals over the entire sand surface for high-ER conditions (Figure 7b).

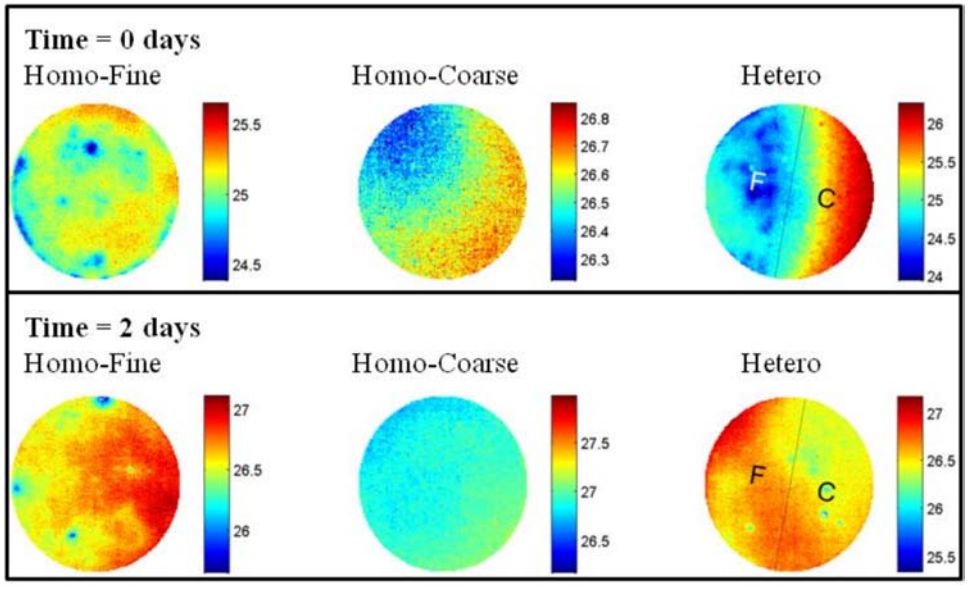

Figure 8. Surface temperature, under low PE conditions, for the fine, coarse and heterogeneous NaCl columns at two time points during the experiment. Due to crust formation, evaporation rates are reduced and surface temperature increases. To increase contrast, each pseudo-colorized scale is different.

low water content. The observed increase in ER (Figure 6) lasted for the first ~4 and ~15 h, for the high- and low-PE conditions, respectively. The vapor pressure gradient between the solution and the precipitated salt crust can potentially explain these enhanced vapor fluxes. Vapor pressure over a saturated NaCl solution is ~75% of the vapor pressure above DI for an equivalent temperature [*Stokes and Robinson*, 1949; *Robinson and Stokes*, 1959; *Sghaier et al.*, 2007]. Vapor pressure at a surface of a NaCl crystal is related to the concentration of the absorbed water on the crystal surface [*Cinkotai*, 1971]. Until the completion of an absorbed water monolayer on the crystal surfaces, the effective vapor pressure in the crystal vicinity is equal to 40% of DI for an identical temperature [*Dai et al.*, 1997; *Hucher et al.*, 1967; *Verdaguer et al.*, 2005]. The crystal will continue absorbing water, as long as its vapor pressure is lower than the ambient vapor pressure. For the case presented here (precipitated NaCl crust some distance above a saturated NaCl solution), the salt crust will absorb water until reaching vapor pressure equal to the vapor pressure immediately above the solution. Theoretically, at the beginning of the process a vapor pressure difference of 35% exists between the solution and the salt crust surfaces. This vapor pressure gradient is likely to create vapor flux from the solution in the porous media below the crust toward the salt crust, thus increasing the ER as observed at the beginning of the process (Figure 6).

[40] As salt crust continuously grows, transport mechanisms become more complex than the process described above since precipitated salt crust must be in contact at some point with the liquid solution otherwise salt crystals would not continue to grow. On the other hand, if the local increase in ER is the result of vapor pressure gradient between the solution and the salt crust, then an air gap has to exists, to allow the phase change of liquid water to vapor. We thus suggest the following mechanistic model to explain the increase in evaporation rate. A porous medium is never perfectly homogeneous; some distribution in particle sizes and pore dimensions are to be expected [*Yanuka et al.*, 1986; *Manwart et al.*, 2000]. Smaller pores in the matrix draw water from the larger pores due to stronger capillary forces [*Lehmann and Or*, 2009; *Lehman et al.*, 2008] pulling water toward the evaporation front while the liquid-gas interface in the larger pores recedes downward into the matrix, as per its corresponding air entry value. The capillary flow suggests that in porous media salt crust nucleation would occur first in the fine pores with highest solution concentration. As salt nucleates and begins to grow and expand it may cover nearby larger pores. As a result, in the larger pores, where the evaporation front is below matrix surface an air gap exists between the solution and the precipitated salt crust. Consequently, the solution is exposed to significant vapor pressure gradients that increases vapor flow from the poresolution toward the salt crust. The salt crust's bottom surface absorbs water until it is saturated and from this point it begins to act as a barrier, decreasing further evaporation fluxes between pore solution and atmosphere. In the experiments presented here, the increase in ER started as evaporation began, reflecting the initially high solution concentration, which resulted in immediate salt precipitation as evaporation started.

[41] Figure 9e shows a schematic of salt crawling from a small pore toward a larger pore, a key element of the conceptual mechanism leading to enhanced vapor transport while salt precipitates at the soil-atmosphere interface. It is important to emphasize that this mechanism is not restricted to what is defined here as heterogeneous porous media. The natural stochastic heterogeneity of any porous media [*Yanuka et al.*, 1986; *Manwart et al.*, 2000] is likely to be enough to produce this effect. In fact, the increase in ER was observed also for the Homo-fine-NaCl column. The salt crawling from nucleation points on the surface was

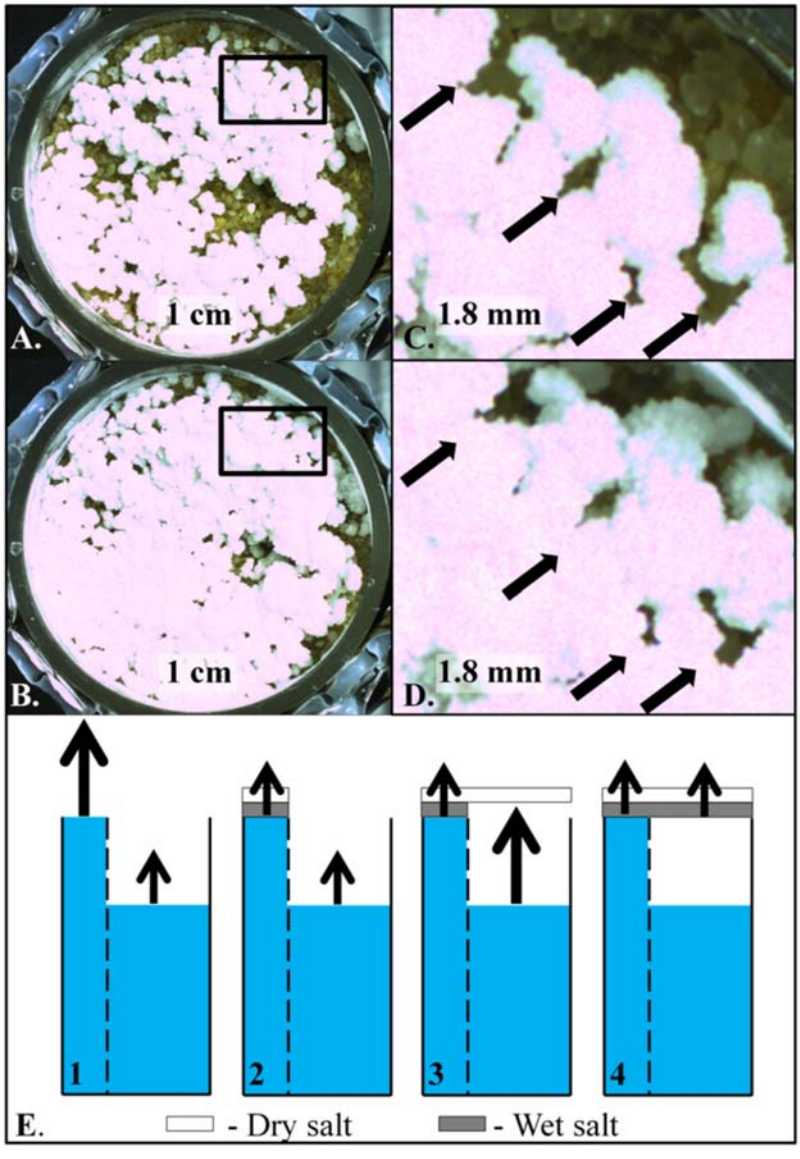

Figure 9. Salt crawling over evaporated porous media with natural distribution of grains and pores dimensions. (a) Subimage and (b) top-view photographs of the evaporated Homo-coarse column, 24 and 48 h after evaporation began, respectively. (c and d) Magnification of the square areas in Figures 9a and 9b. Arrows indicate initial locations of the holes in the salt. (e) Schematically, the conceptual mechanism of the salt crawling from small to large pore and short-term evaporation enhancement mechanism. Initially no salt has precipitated (Figure 7e, 1). Salt nucleates over the fine pores (Figure 7e, 2) and a dry salt grows laterally over the coarser pores, providing a boundary condition for enhanced vapor transport due to the developed vapor pressure gradient (Figure 7e, 3), until salt crust bottom surface is water saturated (Figure 7e, 4). The blue area is saturated with respect to the salty solution and the dashed line separates the fine and coarse pores. Arrows indicate locations of evaporation and arrows lengths correspond to evaporation rates. The white and gray layers (upper and lower, respectively) represent dry and wet salt crusts, respectively.

visually observed for the Homo-coarse column with the water table set at the matrix surface. Salt precipitation was photographed (visible wavelength) 24 h after the evaporation process began. Small holes in the salt crust, which remained open throughout the evaporation process, were used as tracers to follow salt crust motion. It was found that these holes moved sideways. This indicates a salt crystallization pattern of new salt being precipitated at the nucleation centers which pushes away the previously precipitated salt. In the example presented here (Figures 9a–9d) the holes in the salt crust were pushed for a distance of ∼1.5 mm, which is several orders of magnitude larger than the average pore dimension (Table 1), yet not big enough to affect the IRT analysis which assumed vertical growth of the salt above the evaporating surface. The lateral direction of salt crystals growth could simply reflect gravitational balance.

[42] In this work and several other studies [e.g., *Acero et al.*, 2007; *Fujimaki et al.*, 2006; *Nachshon et al.*, 2011;

Nassar and Horton, 1999; *Shimojima et al.*, 1996] it was assumed that evaporation takes place below the salt crust and that water vapor passes through the salt crust by diffusion. The dry salt crust assumption is also relevant for a technical reason as the interpretation of the IRT readings assumed dry salt crust conditions. The good agreement between IRT and the mass balance results, and the enhanced ER which is explained by the vapor pressure gradient driven mechanism, lends credence to the dry salt crust assumption. It was also reported in literature [*Dai et al.*, 1995; *Foster and Ewing*, 2000; *Rodriguez-Navarro and Doehne*, 1999; *Peters and Ewing*, 1997] that NaCl absorbs water on the crystal surface, while the crystal inner volume is dry. *Foster and Ewing* [2000] reported that the absorbed water at the crystal's surface acts as liquid water which then can diffuse (as vapor) through the salt crust toward the atmosphere.

[43] Lastly, to confirm that the reduction in evaporation was due to the NaCl crust formation and not due to internal precipitation within matrix pores, the salt crust was mechanically peeled off periodically (every 24 h) from the top of the Homo-fine column. The ER mostly recovered after peeling the crust, and was then followed by a gradual decrease in evaporation as new crust formed (Figure 10). The SS1 stage is not distinguishable from the recovery stage as solution is already saturated in respect to NaCl and salt precipitation starts immediately after peeling. SS3 evaporation rate values at the end of every peeling cycle remained relatively constant (0.25 ± 0.05 cm d^{-1}), while peak recovery ER (part of SS1) gradually increased following each peeling cycle.

[44] The increase in peak ER recovery with each peeling cycle is peculiar. Maximum ER was observed for the last peeling cycle (2.2 cm d^{-1}). This value is lower than the maximum value evaporating from the Homo-fine DI column (3 cm d^{-1}), with the difference consistent with the reduction in vapor pressure corresponding to a saturated NaCl solution. The consistently increasing recovery peak ER suggests an additional interesting mechanism unique to saline evaporation. Assuming solution concentration is at saturation throughout the experiment, and that peeling removes the salt crust completely, then, a stepwise increase in ER might reflect a stepwise increase in water content at the matrix surface. The gradually blocked vapor transport below the crust may result in condensate and increase in water content below the salt crust. The condensed water may dilute the solution concentration just below the salt crust as proposed by *Gran et al.* [2011b]. Consequently, it can decrease solution osmotic potential, thus increasing solution vapor pressure just below the salt crust, which might be another contributor for the observed increasing in ER. As the salt crust is removed, this condensed water is exposed to evaporation and the surface partially dries out. Hence, pores that were dry in previous cycle may become partially saturated and a hysteresis cycle begins of drying and wetting after every peeling. With subsequent peeling cycles the water content of the initially dry pores increases until reaching saturation as observed by the ER measurements of the last peeling cycle. SS1 ER for the fine sand sections of the Hetero columns (for high PE) was in the range of 2–2.5 cm d^{-1} (Figures 6c and 6d), but for the Homo-fine SS1 ER was 1 cm d^{-1} (Figure 6a). If we further assume that the Hetero fine section ER corresponds to full saturation (water content), the lower Homo-fine ER indicates a surface water content which is approximately 50% drier. The gradual increase in ER after every peeling and the fact that the maximal ER does not pass the maximal possible ER for these experimental conditions, suggests that there is gradual increase in Homo-fine surface water content between the peelings. Quantification and strict proof of this process is beyond the scope of this manuscript, and will require future study with detailed water content and salinity measurements of the near salt crust region.

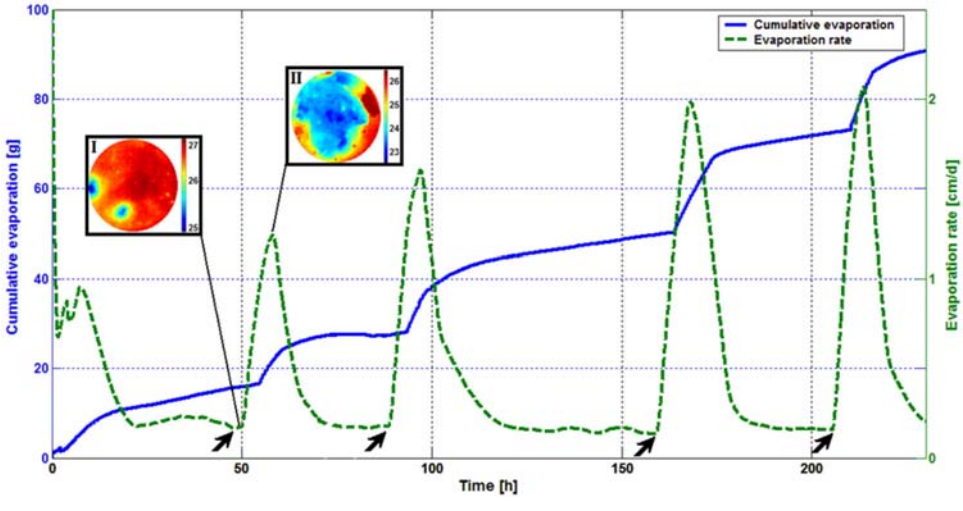

Figure 10. Cumulative evaporation and evaporation rates from Homo-fine-NaCl column for the peeling experiment. Arrows indicate peeling events, which are immediately followed by a jump in evaporation rate. Images I and II are thermal images of the column from the IRT taken at the time noted by the pointer line. Image I was taken after the salt crust precipitated; and image II was taken just after salt crust peeling. The average temperatures of the column surfaces are 26.5 and 23.5°C for I and II, respectively, corresponding to evaporation rates of 0.25 and 1.25 cm d^{-1}, respectively.

4.3. Evaporation From NaI Columns

[45] As mentioned above, NaI was chosen due to its tendency for subflorescent precipitation [*Nachshon et al.*, 2011]. The initial concentration of the NaI solution concentration was half of NaI solubility limit. Therefore, reduction in ER associated with physical barriers due to salt precipitation is expected to be delayed as compared with NaCl samples that were at the solubility limit from the outset. In addition to vapor pressure reduction due to the increase in NaI concentration during evaporation, increase in solution viscosity also leads to decreased vapor pressure [*Grinnell and Dole*, 1929]; both of these mechanisms result in ER reduction [*Lehmann et al.*, 2008; *Salhotra et al.*, 1985]. *Nachshon et al.* [2011] showed using CT scans that NaI precipitates within near-surface pores (top 1–2 cm of the matrix). Subflorescent precipitation reduces matrix porosity, but the matrix surface remains in contact with the atmosphere. Therefore, any changes in ER by the precipitated salt would be related to the effect of vapor pressure suppression and pore clogging on capillary permeability. The lack of efflorescent salt crust should also eliminate the process of osmotically driven enhancement in vapor flow which was observed for the NaCl columns.

[46] Figure 11 presents ER measurements for NaI columns under high- and low-PE conditions, from which it can be seen that NaI does not exhibit the same phenomenological behavior seen for NaCl, including the distinct three saline stages of evaporation. The lack of osmotically driven decrease is likely due to the low level of solution concentration (relative to saturation) that was used. For low PE conditions ER maintains a reduced but constant value throughout the experiment. For high-PE conditions a notable reduction in ER was observed after 25 and 33 h, for the Homo-fine and fine sand section in the Hetero column, respectively. This is in contrast to the NaCl columns, where precipitated NaCl affected evaporation immediately as evaporation began. As mentioned, this disparity is expected, and it reflects high solubility of NaI and the low initial solution concentration which resulted in postponed NaI crystallization onset, allowing undisturbed capillary flow of the solution for relatively long durations. From CT scans of the NaI column (Figure 12) it is evident that salt crystals were precipitated mainly in the small pores. Since NaI precipitation occurred below the surface it is impossible to determine when salt precipitation began. Consequently, it is hard to separate between solution concentration (osmotic potential and viscosity) and salt precipitation effects on ER reduction. Nevertheless, the total effect of these mechanisms was measured. For the high-PE conditions salinity reduced the solution flow by maximum value of 15% for the Homo-fine column. A smaller reduction in ER in the range of 2% was observed for the Hetero column, under high-PE conditions. For low-PE conditions, the initial ER was too small to be affected by the solution concentration or to precipitate sufficient salt mass to limit the solution capillary flow.

[47] Figure 12 presents CT scans of a subsample of the Hetero NaI column following completion of the low ER experiment. CT images indicate that most of the salt was precipitated within the fine sand section. Mass precipitated in the fine portion was about 10 times greater than in the coarse portion.

5. Conclusions

[48] We studied spatial and temporal effects of salt precipitation on evaporation from homogeneous and heterogeneous porous media. By maintaining constant hydraulic head and atmospheric demand, specific effects of salt precipitation on evaporation dynamics were elucidated. The use of IRT enabled separation of the contributions to evaporation from different textural domains of a heterogeneous column and helped link thermal signatures of phase change below growing salt crusts. Visual observations and CT

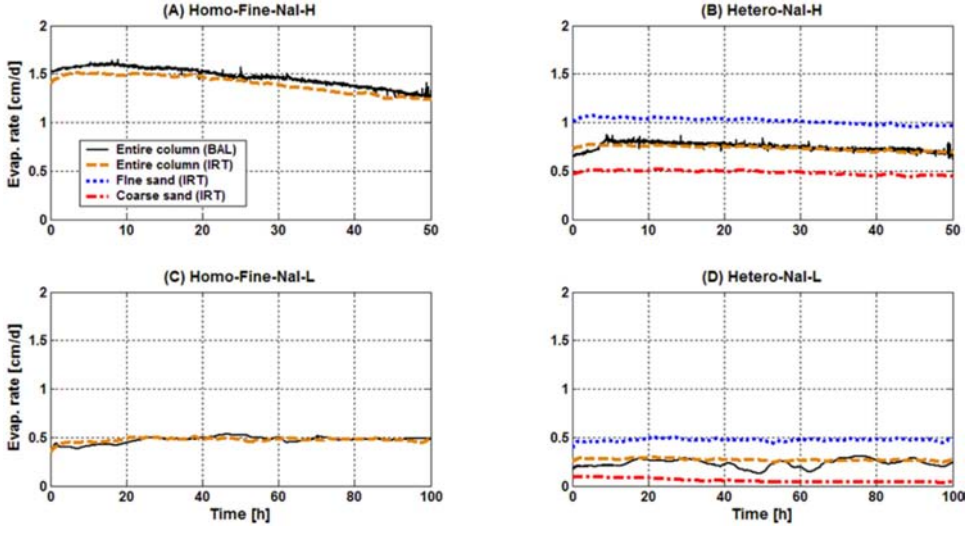

Figure 11. Evaporation rates for NaI columns. Reduction in evaporation rate is moderate and linear, reflected in an increase in solution concentration and a subsequent increase in the poresolution viscosity and its osmotic potential, as well as a minor effect of the precipitated salt within the pores on the hydraulic conductivity of the samples.

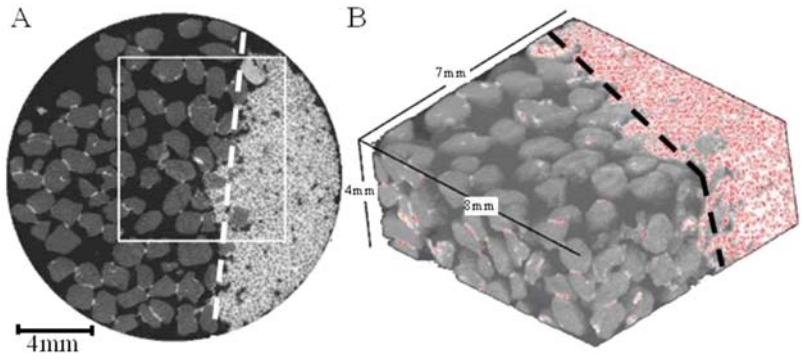

Figure 12. (a) CT scan of the heterogeneous NaI column (view from above). Scan was taken ~1 mm below surface. Black regions are voids, dark gray are sand grains and light gray is the precipitated NaI. White square indicates area presented in Figure 12b. (b) 3-D visualization of the fine-coarse interface area for the NaI heterogeneous column. White material, emphasized with red contours is the precipitated NaI. Dashed line indicates fine and coarse sands interface. The preferential accumulation of the salt between fine grains (right side of image) is evident.

imaging were used to inspect surface and internal matrix salt precipitation patterns. Two salt types were tested, NaCl and NaI, to explore effects of efflorescent and subflorescent precipitation, respectively, on evaporation dynamics.

[49] In agreement with current theory for heterogeneous structures, most of the evaporation occurred from fine sand sections with more than 90% of salt accumulating in or above the small pore sections. Consequently, ER from the fine texture was reduced by almost an order of magnitude, while from the coarser texture, which was relatively free of salt, ER was reduced by at most 50%. *Nachshon et al.* [2011] defined three stages for saline solution evaporation from soils with receding drying front: SS1, SS2 and SS3, which were stated to not necessarily depend on hydraulic conditions but instead on salt precipitation conditions. These stages were evident even under conditions of constant hydraulic head, but only for salt exhibiting efflorescent precipitation. These stages are the product of a number of mechanisms including: increase of solution osmotic potential, salt crust formation (mulching effect), enhanced vapor transport, and condensation effects within coarser portions of a heterogeneous matrix.

[50] The reduction in evaporation rates by salt crust precipitation, despite hydraulic continuity between the solution and the precipitated salt crust, supports the assumption that evaporation occurs below the salt crust and not on top of it as proposed by *Sghaier and Prat* [2009]. The vapor diffusion coefficient through the salt crust depends on salt precipitation pattern which is strongly affected by environmental conditions, specifically the potential evaporation rate. High–potential evaporation conditions produced denser efflorescent crusts that exhibited higher resistance to vapor transport. High–potential evaporation conditions resulted in precipitation of amorphous and homogeneously distributed salt crystals over the evaporating media. Consequently, for these conditions, the media was uniformly sealed by the precipitated salt crust. For low potential evaporation conditions, salt was precipitated in larger, well organized crystals, resulting in portions of the matrix surface that were free of salt, allowing faster vapor diffusion toward the atmosphere. The average vapor diffusion coefficient for low potential evaporation conditions was double that for high–potential evaporation conditions.

[51] A short period of increasing ER was observed during the beginning of first stage of evaporation for the NaCl experiments. The proposed mechanism is enhanced vapor transport through coarser air-filled pores toward the salt crust due to a vapor pressure gradient between the salt crust on the surface and pore solution further down. This process is facilitated by salt crust that initially precipitates over small, saturated pores, laterally crawling from these nucleation centers and partially covering dry larger pores. The peelings of the NaCl salt crust showed that the efflorescent precipitated salt had no effect on the pores within the matrix and it only reduced evaporation due to mechanical clogging of the upper boundary of the matrix. A gradual increase in maximal evaporation rates was observed after every peeling of the salt crust, indicating a gradual increase in near-surface matrix water content. We suggest that a pumping mechanism is induced by the precipitation and peeling cycle of the salt crust. The pumping mechanism is driven by the vapor pressure gradient between the pore solution and the salt crust. As vapor concentration increases below the salt crust, part of the vapor condenses, thus increasing water content in that region. When the salt crust is removed, the higher water content results in higher hydraulic conductivity, and hence, higher evaporation rates.

[52] This study sheds new light on the interactions between evaporation and salt precipitation at the pore scale for homogeneous and heterogeneous porous media. Different mechanisms were proposed in here to explain changes in evaporation process, depending on whether salt deposits as efflorescence or subflorescence. For subflorescence the key mechanism is pore clogging, and depending on initial concentration it is also influenced by osmotic and viscous effects. For efflorescent precipitation, key mechanisms include the salt mulching and internal vapor transport processes through partially dry media. The proposed mechanisms of vapor transport between the solution and the precipitated salt crust, due to vapor pressure gradients; salt crawling

theory; and the assumption that evaporation takes place below the salt crust should be further explored in the future.

Notation

A	Surface area (m^2)
c	Saline solution concentration by volume (cm^3 cm^{-3})
C_s	Vapor concentration difference (Kg m^{-3})
D	Characteristic length (diameter) of sand columns (m)
D_{air}	Vapor diffusion coefficient in air (m^2 s^{-1})
D_s	Vapor diffusion coefficient in salt crust (m^2 s^{-1})
e_0	Evaporation rate (m s^{-1})
h_a	Convective heat transfer coefficient (W m^{-2} K)
J	Vapor mass flux (Kg s^{-1})
K_a	Heat conductivity of the ambient air (W m^{-1} K)
K_{salt}	Heat conductivity of the salt crust (W m^{-1} K)
K_{sand}	Heat conductivity of the sand (W m^{-1} K)
L_{cap}	Height difference in water level between the fine and coarse sands (m)
L_w	latent heat of vaporization (J kg^{-1})
Nu	Nusselet number
Pr	Prandtl numbers
$Q_{\text{conduction}}$	Conductive energy flux (W m^{-2})
$Q_{\text{convection}}$	Convective energy flux (W m^{-2})
$Q_{\text{evaporation}}$	Energy flux due to evaporation (W m^{-2})
R	Radius of sand columns (m)
r	Average pores radius (m)
Re	Reynolds number
t	Time (s)
T	Generic Temperature (K)
T_∞	Ambient air temperature (K)
$T_{\text{coarse sand}}$	Coarse sand surface temperature (K)
$T_{\text{fine sand}}$	Fine sand surface temperature (K)
T_{salt}	Salt surface temperature (K)
T_{sand}	Volume averaged temperature of sand (K)
ΔL_{salt}	Salt crust thickness (m)
ϕ_{r}	Residual water content (cm^3 cm^{-3})
ϕ_{s}	Porosity (cm^3 cm^{-3})
ρ_{water}	Water density (Kg m^{-3})
ρ	averaged partially saturated soil density (kg m^{-3})

[53] **Acknowledgments.** This work was mostly funded by the Binational Science Foundation (BSF), contract 2006018. ES and DO gratefully acknowledge funding by the Swiss National Science Foundation project 2000021-113676/1, by the German Research Foundation DFG project (FOR 1083) Multi-Scale interfaces in Unsaturated Soil (MUSIS) and the generous assistance of Daniel Breitenstein and Peter Lehmann in various aspects of the study. Comments provided by three anonymous reviewers helped to improve this manuscript.

References

Acero, P., C. Ayora, and J. Carrera (2007), Coupled thermal, hydraulic and geochemical evolution of pyritic tailings in unsaturated column experiments, *Geochim. Cosmochim. Acta*, *71*, 5325–5338.

Alberty, R. A. (1987), *Physical Chemistry*, 7th ed., John Wiley, New York.

Anderson, N. G. (2000), *Practical Process Research and Development*, 1st edition, pp. 354, Academic Press, San Diego, Calif.

Beauheim, R. L., and M. R. Randall (2002), Hydrology and hydraulic properties of a bedded evaporative formation, *J. Hydrol*, *259*, 1–4, 66–88, doi:10.1016/S0022-1694(01)00586-8.

Ben-Asher, J., A. D. Matthias, and A. W. Warrick (1983), Assessment of evaporation from bare soil by infrared thermometry, *Soil Sci. Soc. Am. J.*, *47*, 185–191.

Bird, R. B., W. E. Steward, and E. N. Lightfoot (2007), *Transport Phenomena*, 2nd edition, pp. 905, John Wiley, New York.

Blight, G. E. (2002), Measuring evaporation from soil surfaces for environmental and geotechnical purposes, *Water SA*, *28*, 381–394.

Casas, E., and T. K. Lowenstein (1989), Diagenesis of saline pan Halite: Comparison of petrographic features of modern, quaternary and permian Halites, *J. Sediment. Petrol.*, *59*, 724–739.

Chen, X. Y. (1992), Evaporation from a salt-encrusted sediment surface: Field and laboratory studies, *Aust. J. Soil Res.*, *30*, 429–442.

Cinkotai, F. F. (1971), The behavior of sodium chloride particles in moist air, *J. Aerosol. Sci.*, *2*, 325–329, doi:10.1016/0021-8502(71)90057-7.

Daamen, C. C., and L. P. Simmonds (1995), Measurement of evaporation from bare soil and its estimation using surface resistance, *Water Resour. Res.*, *32*, 225–242.

Dai, J. D., J. S. Peters, and E. G. Ewing (1995), Water adsorption and dissociation on NaCl Surfaces, *J. Phys. Chem.*, *99*, 10299–10304.

Dai, Q., J. Hu, and M. Salmeron (1997), Adsorption of water on NaCl (100) surfaces: Role of atomic steps, *J. Phys. Chem. B*, *101*, 1994–1998.

Evett, S. R., A. D. Matthias, and A. W. Warrick (1994), Energy balance model of spatially variable evaporation from bare soil, *Soil Sci. Soc. Am. J.*, *58*, 1604–1611.

Fick, A. (1855), Ueber Diffusion, *Ann. Phys. Chem.*, *170*, 59–86.

Fisher, R. A. (1923), Some factors affecting the evaporation of water from soil, *J. Agron. Sci.*, *13*, 121–143.

Foster, C. M., and G. E. Ewing (2000), Adsorption of water on the NaCl (001) surface. II. An infrared study at ambient temperatures, *J. Chem. Phys.*, *112*(15), 6817–6826.

Fujimaki, H., T. Shimano, M. Inoue, and K. Nakane (2006), Effect of a salt crust on evaporation from a bare saline soil, *Vadose Zone J.*, *5*, 1246–1256.

Gran, M., J. Carrera, J. Massana, M. W. Saaltink, S. Olivella, C. Ayora, and A. Lloret (2011a), Dynamics of water vapor flux and water separation processes during evaporation from a salty dry soil, *J. Hydrol.*, *396*, 215–220, doi:10.1016/j.jhydrol.2010.11.011.

Gran, M., J. Carrera, S. Olivella, and M. W. Saaltink (2011b), Modeling evaporation processes in a saline soil from saturation to oven dry conditions, *Hydrol. Earth Syst. Sci. Discuss.*, *8*, 529–554, doi:10.5194/hessd-8-529-2011:2011.

Grinnell, J., and M. Dole (1929), The viscosity of aqueous solutions of strong electrolytes with special reference to Barium Chloride, *J. Am. Chem. Soc.*, *51*(10), 2950–2964, doi:0.1021/ja01385a012.

Hucher, M., A. Oberlin, and R. Holart (1967), Adsorption of water vapor on the cleavage surfaces of some alkali metal halides, *Bull. Soc. Franc. Mineral. Crist. 90*, 320–332.

Kamai, T., N. Weisbrod, and M. I. Dragila (2009), Impact of ambient temperature on evaporation from surface-exposed fractures, *Water Resour. Res.*, *45*, W02417, doi:10.1029/2008WR007354.

Kelly, S. F., and J. S. Selker (2001), Osmotically driven water vapor transport in unsaturated soils, *Soil Sci. Soc. Am. J.*, *65*, 1634–1641.

Kimball, B. A., R. D. Jackson, R. J. Reginato, F. S. Nakayama, and S. B. Idso (1976), Comparison of field measured and calculated soil heat fluxes, *Soil Sci. Soc. Am. J.*, *40*, 18–25.

Lehmann, P., and D. Or (2009), Evaporation and capillary coupling across vertical textural contrasts in porous media, *Phys. Rev. E*, *80*(4), 046318, doi:10.1103/PhysRevE.80.046318.

Lehmann, P., S. Assouline, and D. Or (2008), Characteristic lengths affecting evaporative drying of porous media, *Phys. Rev. E.*, *77*, 056309, doi:10.1103/PhysRevE.77.056309.

Manwart, C., S. Torquato, and R. Hilfer (2000), Stochastic reconstruction of sandstones, *Phys. Rev. E*, *62*(1), 893–899, doi:10.1103/PhysRevE.62.893.

Millington, R. J., and J. P. Quirk (1961), Permeability of porous solids, *Trans. Faraday Soc.*, *57*, 1200–1207.

Mullin, J. W. (2001), *Crystallization*, 4th edition, pp. 302, Academic Press, San Diego, Calif.

Nachshon, U., N. Weisbrod, M. I. Dragila, and A. Grader (2011), Combined evaporation and salt precipitation in homogeneous and heterogeneous porous media, *Water Resour. Res.*, *47*, W03513, doi:10.1029/2010WR009677.

Nassar, I. N., and R. Horton (1999), Salinity and compaction effects on soil water evaporation and water and solute distributions, *Soil Sci. Soc. Am. J.*, *63*, 752–758.

Penman, H. L. (1948), Natural evaporation from open water, bare soil and grass, *Proc. R. Soc. London*, *193*, 120–145.

Peters, A. J., and E. Ewing (1997), Water on Salt: An infrared study of adsorbed H_2O on NaCl(100) under ambient conditions, *J. Phys. Chem. B*, *101*(50), 10880–10886.

Polak, A., A. S. Grader, R. Wallach, and R. Nativ (2003), Chemical diffusion between a fracture and the surrounding matrix: Measurement by computed tomography and modeling, *Water Resour. Res.*, *39*(4), 1106, doi:10.1029/2001WR000813.

Press, F., and R. Siever (1986), *Earth*, 4th edition, pp. 309–312, Freeman, New York.

Robinson, R. A., and R. H. Stokes (1959), *Electrolyte Solutions*, 2nd edition, Butterworths Sci. Publ., London.

Rodriguez-Navarro, C., and E. Doehne (1999), Salt weathering: Influence of evaporation rate, supersaturation and crystallization pattern, *Earth Surf. Processes Landforms*, *24*(3), 191–209.

Salhotra, A. M., E. E. Adams, and D. R. F. Harleman (1985), Effect of salinity and ionic composition on evaporation: Analysis of Dead Sea evaporation pans, *Water Resour. Res.*, *21*, 1336–1344.

Schwartz, A. M., and A. S. Myerson (2002), Solutions and solution properties, in *Handbook of Industrial Crystallization*, 2nd edition, edited by A. S. Myerson, p. 2013, Butterworth-Heinemann, Woburn, doi:10.1016/B978-075067012-8/50003-3.

Scotter, D. R., and P. A. C. Raats (1970), Movement of salt and water near crystalline salt in relatively dry soil, *Soil Sci.*, *109*, 170–178.

Sghaier, N., and M. Prat (2009), Effect of efflorescence formation on drying kinetics of porous media, *Transport Porous Med.*, *80*, 441–454, doi:10.1007/s11242-009-9373-6.

Sghaier, N., M. Prat, and S. Ben Nasrallah (2007), On ions transport during drying in a porous medium, *Transp. Porous Med.*, *67*, 243–274, doi:10.1007/s11242-006-9007-1.

Shahraeeni, E., and D. Or (2010), Thermo-evaporative fluxes from heterogeneous porous surfaces resolved by infrared thermography, *Water Resour. Res.*, *46*, W09511, 10.1029/2009WR008455.

Shahraeeni, E., and D. Or (2011), Quantification of subsurface thermal regimes beneath evaporating porous surfaces, *Int. J. Heat Mass Trans.*, *54*, 4193–4202, doi:10.1016/j.ijheatmasstransfer.2011.05.024.

Shimojima, E., R. Yoshiokab, and I. Tamagawa (1996), Salinization owing to evaporation from bare-soil surfaces and its influences on the evaporation, *J. Hydrol.*, *18*, 109–136.

Stokes, R. H., and R. A. Robinson (1949), Standard solutions for humidity control at 25°C, *Ind. Eng. Chem.*, *41*, 2013, doi:10.1021/ie50477a041.

Valeriani, C., E. Sanz, and D. Frenkel (2005), Rate of homogeneous crystal nucleation in molten NaCl, *J. Chem. Phys.*, *122*, 194501, doi:10.1063/1.1896348.

Van Wesemael, B., J. Poesen, C. S. Kosmas, N. G. Danalatos, and J. Nachtergaele (1996), Evaporation from cultivated soils containing rock fragments, *J. Hydrol.*, *182*, 65–82.

Verdaguer, A., G. M. Sacha, M. Luna, D. F. Ogletree, and M. Salmeron (2005), Initial stages of water adsorption on NaCl (100) studied by scanning polarization force microscopy, *J. Chem. Phys.*, *123*, 124703-1–124703-8, doi:10.1063/1.1996568.

Weisbrod, N., R. M. Niemet, T. McGinnis, and J. S. Selker (2003), Water vapor transport in the vicinity of imbibing saline solutions: Homogenous and layered systems, *Water Resour. Res.*, *39*(6), 1145, doi:10.1029/2002WR001539.

Weisbrod, N., Pillersdorf, M., Dragila, M., Graham, C., Cassidy, J., and C. A. Cooper (2005), Evaporation from fractures exposed at land surface: Impact of gas-phase convection on salt accumulation, in *Dynamics of Fluids and Transport in Fractured Rock.*, Geophys. Monogr. Ser, vol. *162*, edited by B. Faybishenko, P. A. Witherspoon, and J. Gale, pp. 151–164, AGU, Washington, D. C.

White, F. M. (1991), *Viscous Fluid Flow*, pp. 614, McGraw-Hill, New York.

Wissmeier, L., and D. A. Barry (2008), Reactive transport in unsaturated soil: Comprehensive modeling of the dynamic spatial and temporal mass balance of water and chemical components, *Adv. Water Resour.*, *31*, 858–875, doi:10.1016/j.advwatres.2008.02.003.

Yanuka, M., F. A. L. Dullien, and D. E. Elrick (1986), Percolation processes and porous media: I. Geometrical and topological model of porous media using a three-dimensional joint pore size distribution, *J. Colloid Interface Sci.*, *112*(1), 24–41, doi:10.1016/0021-9797(86)90066-4.

Zhu, W. C., J. Liu, D. Elsworth, A. Polak, A. Grader, J. C. Sheng, and J. X. Liu (2007), Tracer transport in a fractured chalk: X-ray CT characterization and digital-image-based (DIB) simulation, *Transp. Porous Media*, *70*(1), 25–42, doi:10.1007/s11242-006-9080-5.

M. Dragila, Faculty of Soil Science, School of Integrated Plant, Soil and Insect Sciences, Oregon State University, 3135 Ag Life Sciences Bldg., Corvallis, OR 97331, USA.

U. Nachshon and N. Weisbrod, Department of Environmental Hydrology and Microbiology, Zuckerberg Institute for Water Research, Jacob Blaustein Institutes for Desert Research, Ben-Gurion University of the Negev, Sede Boker Campus, 84990, Midreshet Ben-Gurion, Israel. (weisbrod@bgu.ac.il)

D. Or and E. Shahraeeni, Institute of Terrestrial Ecosystems, Department of Environmental Science, ETH Zurich, CH-8092 Zurich, Switzerland.